



# A versatile single-copper-atom electrocatalyst for biomass valorization

Yongfang Zhou<sup>a</sup>, Thomas J.A. Slater<sup>d</sup>, Xuanli Luo<sup>e</sup>, Yi Shen<sup>a,b,c,\*</sup>

<sup>a</sup> School of Food Science and Engineering, South China University of Technology, Guangzhou 510641, China

<sup>b</sup> Overseas Expertise Introduction Center for Discipline Innovation of Food Nutrition and Human Health (111 Center), Guangzhou 510641, China

<sup>c</sup> China-Singapore International Joint Research Institute, Guangzhou Knowledge City, Guangzhou 510663, China

<sup>d</sup> Electron Physical Sciences Imaging Centre, Diamond Light Source Ltd., Oxfordshire OX11 0DE, UK

<sup>e</sup> Advanced Materials Research Group, Faculty of Engineering, University of Nottingham, Nottingham NG7 2RD, UK

## ARTICLE INFO

### Keywords:

Electro-oxidation  
Single copper atom electrocatalyst  
Biomass conversion  
Operando electrochemical Raman spectra

## ABSTRACT

Single atom electrocatalysts (SAECs) exhibit intriguing catalytic performance due to their utmost atom-utilization efficiency and unique electronic structure. However, the application of SAECs is limited on simple reactions such as the hydrogen/oxygen evolution reactions, and oxygen/nitrogen reduction reactions. Herein, single copper atoms supported on nitrogen doped carbon nanosheets (Cu/NCNSs) were demonstrated as a versatile SAEC for biomass upgrade. The activity of Cu/NCNSs was benchmarked against commercial Cu nanoparticles. Twelve basic platform compounds including 5-hydroxymethylfurfural (HMF), furfural, glucose, formaldehyde, methanol, ethanol, isopropanol, ethylene glycol, glycerol, benzyl alcohol, formic acid, and oxalic acid were employed as substrates. The products of electro-oxidation of these substrates were analyzed by high performance liquid chromatography. The reaction pathways and mechanisms of substrate oxidation on Cu/NCNSs and Cu NPs were explored by in-situ electrochemical Raman spectra. HMF oxidation on Cu NPs followed the 5-diformylfuran (DFF) path at lower potentials, while it turned to 5-hydroxymethyl-2-furancarboxylic acid path at applied potentials over 1.67 V. For Cu/NCNSs, HMF oxidation followed the alcohol hydroxyl oxidation pathway, that is, the direction of generating DFF. The active sites for substrate oxidation on Cu/NCNSs are different from those on Cu NPs. This work broadened the application of SAECs in the field of biomass upgrade, and paved a new route to fabricate advanced electrocatalysts for biomass valorization.

## 1. Introduction

As effects of fossil fuel consumption are increasingly prevalent, developing renewable energy technologies is particularly important [1, 2]. Electrochemical oxidation of biomass-derived feedstocks is considered as a promising approach for sustainable energy development [3–5]. Biomass, a type of renewable non-fossil resource, can be selectively oxidized into many value-added products [6–8]. The valorization of biomass to high value-added products or intermediates for fine chemical synthesis may be a promising route to fulfill sustainable energy landscape. For instance, the oxidation of 5-hydroxymethylfurfural (HMF) can obtain valuable chemicals such as 5-diformylfuran, 5-formyl-2-furancarboxylic acid and 2,5-furandicarboxylic acid [9–12] while the oxidation of glycerol can result in dihydroxyacetone, glyceric acid, formic acid and so on [13]. Additionally, comparing with the oxygen evolution reaction (OER), the electro-oxidation of the small organic molecules could improve the energy efficiency of water splitting for

hydrogen production. In the past years, there has been a renaissance of research interests in biomass utilization owing to the recent advances in electrocatalysis [14–16]. Especially, Ni-, Cu-based electrocatalysts have been studied for biomass oxidation [17,18].

Lately, single atom electrocatalysts (SAECs) are being considered as alternative catalysts for some reactions due to their utmost atom-utilization efficiency, and unique electronic and geometric configuration [19]. It has been demonstrated that SAECs possess extraordinary catalytic performance for some electrochemical processes, such as the hydrogen evolution reaction [20], OER [21], oxygen reduction reaction [22], nitrogen reduction reaction [23], and CO<sub>2</sub> reduction [24]. However, there are few reports on the detailed reaction mechanism of biomass electrocatalysis on the SAECs. Herein, we present a detailed study to fulfill this research gap using a single-copper-atom supported by nano-porous nitrogen doped carbon nanosheets (Cu/NCNSs) as a model SAEC. Twelve basic platform compounds were selected as substrates, including aldehydes (HMF, furfural, glucose and formaldehyde),

\* Corresponding author at: School of Food Science and Engineering, South China University of Technology, Guangzhou 510641, China.

E-mail address: [feishen@scut.edu.cn](mailto:feishen@scut.edu.cn) (Y. Shen).

<https://doi.org/10.1016/j.apcatb.2022.122218>

Received 13 September 2022; Received in revised form 22 November 2022; Accepted 24 November 2022

Available online 26 November 2022

0926-3373/© 2022 Elsevier B.V. All rights reserved.

alcohols (methanol, ethanol, isopropanol, ethylene glycol, glycerol and benzyl alcohol), and acids (formic acid, and oxalic acid). The Cu/NCNSs were benchmarked against commercial copper nanoparticles (Cu NPs). The products of electro-oxidation processes were determined by high-performance liquid chromatography (HPLC) measurements. To investigate the catalytic mechanisms, an operando electrochemical Raman spectra system was constructed to monitor the variations on the active sites during the electrocatalytic process.

## 2. Experimental

### 2.1. Chemicals and materials

5-hydroxymethylfurfural (HMF, 99%, Aladdin Biochemical Technology Co., Ltd), glycerol (GLY, ≥99%, Sinopharm Chemical Reagent Co., Ltd), ethanol (EtOH, AR, Tianjin Jingdong Tianzheng Precision Chemical Reagent Factory), ethylene glycol (EG, ≥99.5%, Jiangsu Qiangsheng Functional Chemical Co., Ltd), furfural (Fur, 99%, Aladdin Biochemical Technology Co., Ltd), 2-furoic acid (2-FA, 98%, Macklin Biochemical Co., Ltd), oxalic acid dihydrate (OA, AR, Jiangsu Qiangsheng Functional Chemical Co., Ltd), D-(+)-glucose (GLU, AR, Aladdin Biochemical Technology Co., Ltd), formic acid (FA, AR, Tianjin Jingdong Tianzheng Precision Chemical Reagent Factory), benzyl alcohol (BA, AR, Tianjin Damao Chemical Reagent Factory), formaldehyde solution (FM, AR, Guangzhou Chemical Reagent Factory), isopropyl alcohol (IA, AR, Tianjin Fuyu Fine Chemical Co., Ltd), methanol (MA, AR, Sinopharm Chemical Reagent Co., Ltd), dihydroxyacetone (DHA, 99%, Aladdin Biochemical Technology Co., Ltd), glyceraldehyde (GALD, 99%, Aladdin Biochemical Technology Co., Ltd), glyceric acid (GLA, 99%, Aladdin Biochemical Technology Co., Ltd), glycolic acid (GA, 99%, Aladdin Biochemical Technology Co., Ltd), glyoxylic acid (GLOA, 98%, Aladdin Biochemical Technology Co., Ltd), 2,5-furandicarboxylic acid (FDCA, 98%, Aladdin Biochemical Technology Co., Ltd), 5-hydroxymethyl-2-furancarboxylic acid (HFCA, 98%, TCI, America), 5-diformylfuran (DFF, 98%, TCI, America), 5-formyl-2-furancarboxylic (FFCA, 98%, TCI, America), ammonium formate (HPLC, Tianjin Kemiou Chemical Reagent Co., Ltd), methanol (HPLC, Yonghua Chemical Co., Ltd), cyanamide (50% H<sub>2</sub>O, 0.25%, methyl formate stabilizer), sodium dodecyl benzene sulfonate (AR, Shanghai Lingfeng Chemical Reagent Co., Ltd), CuCl<sub>2</sub>·2 H<sub>2</sub>O (99%, Guangzhou Chemical Reagent Factory), HCl (36%, Guangzhou Chemical Reagent Factory), and H<sub>2</sub>SO<sub>4</sub> (98%, Guangzhou Chemical Reagent Factory) were used without further purification. KOH (semiconductor grade 99.99%) was purchased from the Macklin Biochemical Co., Ltd. All solutions were prepared with ultrapure water. Glassy carbon electrode (Φ = 3 mm) was purchased from Tianjin Incole Union Technology Co., Ltd. Carbon paper (TGP-H-060) was purchased from the Shanghai Hesen Electric Co., Ltd. Cu NPs with diameters of 60–100 nm was purchased from the Macklin Biochemical Co., Ltd. Commercial nitrogen-doped graphene (N content ~5.0 wt%) was purchased from the Nanjing XFNANO Materials Tech Co., Ltd.

### 2.2. Synthesis of Cu/NCNSs

The Cu/NCNSs was synthesized by a method reported in the authors' previous work with a few modifications [25]. Firstly, 0.4 g of polystyrene nanospheres, 2 mL of cyanamide solution, 1 mL of furfural, 7.6 mL of H<sub>2</sub>O, 2 mL of ethanol, 2 g of sodium dodecyl benzene sulfonate and 0.4 mL of 0.1 M HCl solution were mixed well, and stirred at 60 °C for 24 h. Subsequently, a predetermined volume of copper chloride solution with a concentration of 10 g L<sup>-1</sup> was added and the mixed solution was continuously stirred for another 48 h. After evaporating the water from the solution, the resulting paste was dried at 100 °C for 72 h and then transferred to a tube furnace for pyrolysis. The pyrolysis process was carried out at 900 °C for 4 h in a nitrogen atmosphere. The obtaining sample was denoted as Cu/NCNSs. The Cu content in the sample is 0.29 wt% as determined by inductively coupled plasma mass

spectrometry. For comparison, nitrogen doped carbon nanosheets (NCNSs) free of any metal were also prepared.

### 2.3. Structural characterization

To reveal the morphology of the sample, a microscope (ARM200F JEOL) at the electron Physical Sciences Imaging Centre at Diamond Light Source was used. The elemental composition of the samples was determined by an energy dispersive X-ray (EDX) spectrometer in the transmission electron microscopy (TEM). The X-ray absorption fine structure spectra were recorded from beamline B18 at Diamond Synchrotron Irradiation Facility. The structure of the samples was further verified by X-ray diffraction spectroscopy using a diffractometer (PW1830, Philips). Ex-situ Raman spectra were recorded with a Renishaw Invia system using 532-nm excitation.

### 2.4. Electrochemical measurements

All the electrochemical measurements were performed using a CHI 760E workstation. A glassy carbon electrode, carbon rod and Hg/HgO electrode were used as working, counter and reference electrodes, respectively. The powdered catalyst was deposited onto the electrode using a method reported in the authors' work [13,26]. An H-type cell separated by a Nafion 117 membrane was used for product analysis. A carbon paper with an area of 2 × 2 cm<sup>-2</sup> was used as the working electrode and the loading of the catalyst was 1 mg cm<sup>-2</sup>. 25 mL of 100/10 mM substrate and/or 0.1 M KOH was used as the electrolyte. All the potentials reported in this work were referenced to a reversible hydrogen electrode (RHE) by following equations: E (vs. RHE) = E (vs. Hg/HgO) + 0.098 + 0.059 \*pH. To verify the accuracy of the experimental data, three tests were conducted for each sample and the average value together with error bars were presented. The turnover frequency (TOF) was calculated as follows [12].

$$TOF = \frac{Current/nF}{mol\ of\ active\ sites} \quad (1)$$

where  $F$  is Faraday's constant, current is obtained from LSV tests,  $n$  is the number of electrons, which are 4 and 8/3 for OER and glycerol oxidation reaction (GOR), respectively.

### 2.5. Product analysis

The products of the reactions were analyzed by HPLC (Agilent 1260 Infinity). Two detectors were used, including a diode array detector (DAD) and a refractive index detector (RID). The details of the experimental procedures were reported in the authors' previous work [26–28]. The selectivity ( $S_i$ ) of product was calculated using Eq. (2).

$$S_i = \frac{C_i}{\sum C_i} \quad (2)$$

where  $C_i$  is the concentration of product  $i$ . HMF or GLY conversion (%) was calculated using Eq. (3).

$$HMF\ or\ GLY\ conversion\ (\%) = \frac{mol\ of\ HMF\ or\ GLY\ consumed}{mol\ of\ initial\ HMF\ or\ GLY} \times 100 \quad (3)$$

### 2.6. In-situ electrochemical Raman spectroscopic measurements

In-situ electrochemical Raman spectroscopic measurements were performed with a Renishaw Invia system. A laser with a wavelength of 532 or 633 nm was used as the excitation light source. The catalyst-loaded carbon paper was served as the working electrode, and its effective area is 0.5 cm<sup>-2</sup>. The mass loading of the catalyst power on the carbon paper was 1 mg cm<sup>-2</sup>. A Pt wire and an Ag/AgCl were used as the counter electrode and reference electrode, respectively. The details of

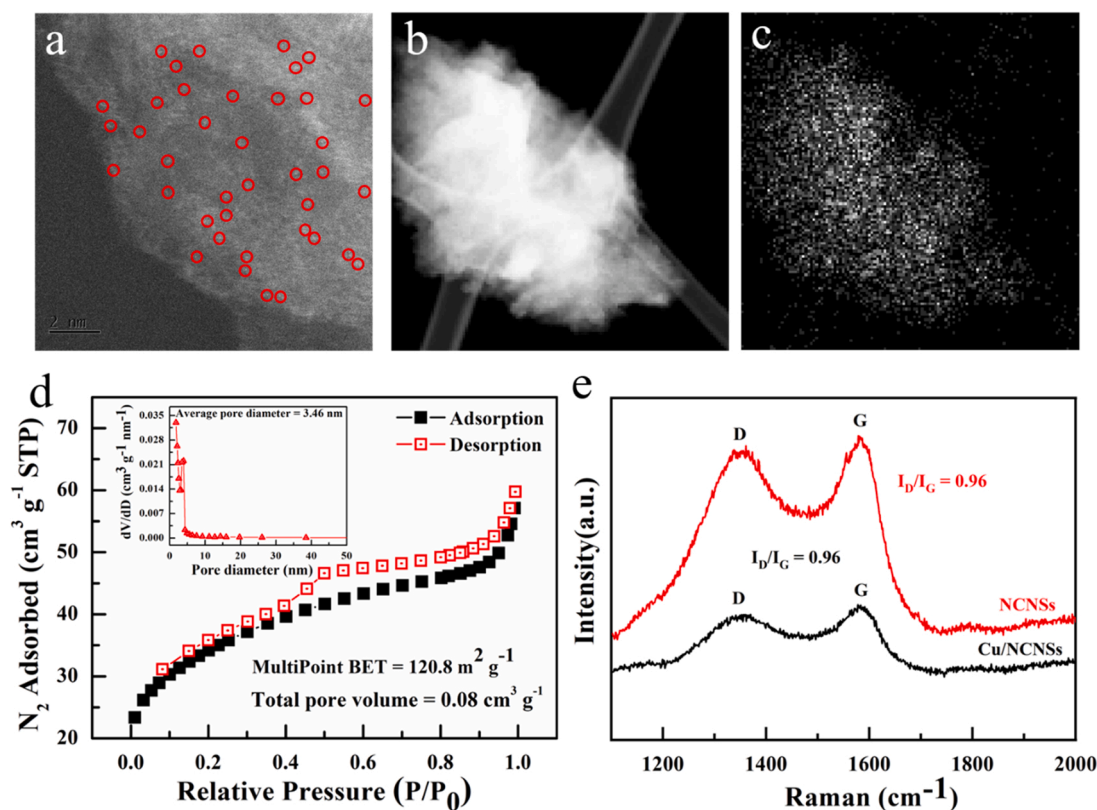


Fig. 1. Structural characterizations of the Cu/NCNSs sample. (a) HAADF-STEM image, (b, c) EDX mapping images, (d)  $N_2$  adsorption-desorption isotherm (the inset is the corresponding pore size distribution), and (e) Raman spectra of Cu/NCNSs and NCNSs.

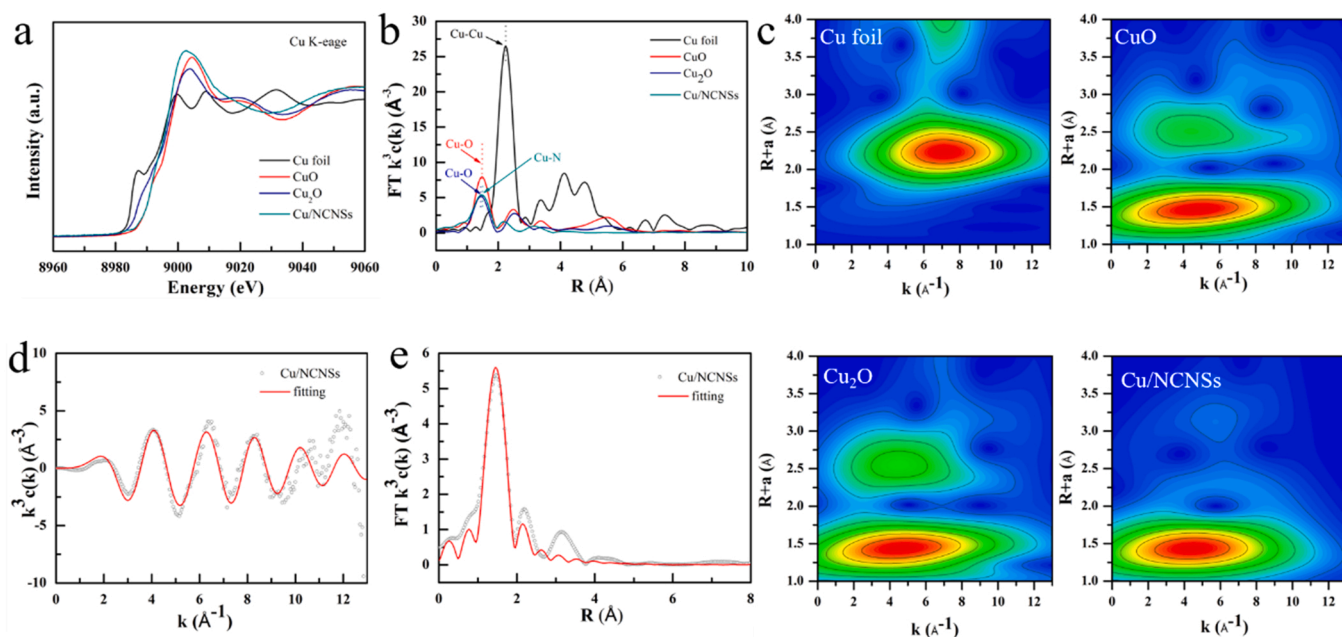


Fig. 2. Analysis of the element-selective X-ray absorption fine structure. (a) Cu K-edge XANES spectra. (b) FT-EXAFS spectra. (c) WT-EXAFS spectra. (d) and (e) corresponding EXAFS fitting curves in  $k$  and  $R$  space, respectively.

the experimental procedures can be found in the authors' previous work [5].

### 3. Results and discussion

#### 3.1. Structural characterization

The representative aberration-corrected high-angle annular dark field (HAADF)-STEM images of the Cu/NCNSs shows numerous bright

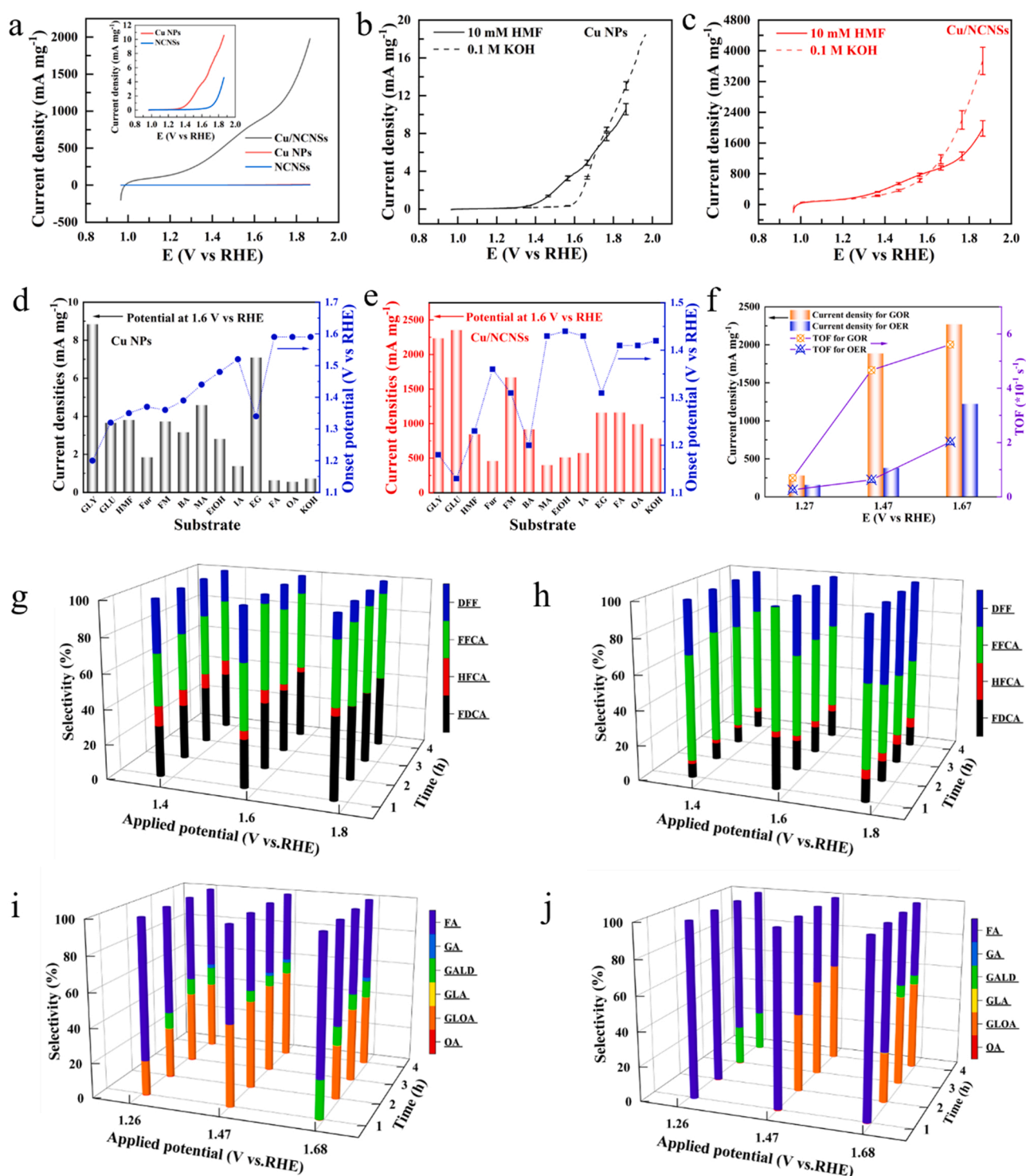


**Fig. 3.** Electrocatalytic performance of Cu/NCNSs and Cu NPs. (a) LSV curves of Cu/NCNSs, Cu NPs and NCNSs in 0.1 M KOH + 10 mM HMF solutions. The inset is a magnifying image. LSV curves of (b) Cu NPs and (c) Cu/NCNSs in 10 mM HMF and/or 0.1 M KOH solutions. Comparison of current densities and onset potentials for the twelve compounds oxidation on (d) Cu NPs and (e) Cu/NCNSs. (f) Current densities and TOF values of GOR and OER at three applied potentials. Product selectivities of HMFOR on (g) Cu NPs and (h) Cu/NCNSs in 0.1 M KOH + 10 mM HMF solutions. Product selectivities of GOR on (i) Cu NPs and (j) Cu/NCNSs in 0.1 M KOH + 100 mM GLY solutions.

dots as highlighted by red circles (see Fig. 1a), which corresponds to the isolated Cu atoms. The EDX mapping images shown in Fig. 1b and c reveal a uniform distribution of Cu elements. It should be pointed out that the sample was thoroughly examined by TEM. No Cu nanoparticles were found in the sample. The structures of Cu/NCNSs were studied by XRD (see Fig. S1). The XRD patterns of the Cu/NCNSs and NCNSs display

three peaks related to graphite carbon. No peaks associated with metallic Cu were noted from the XRD pattern of the Cu/NCNSs, indicating the absence of Cu nanoparticles in the sample. Notably, some small peaks are observed from the XRD pattern of the Cu/NCNSs, which are ascribed to the silicate impurities resulted from the quartz tube during the calcination process. The N<sub>2</sub> adsorption-desorption curve of



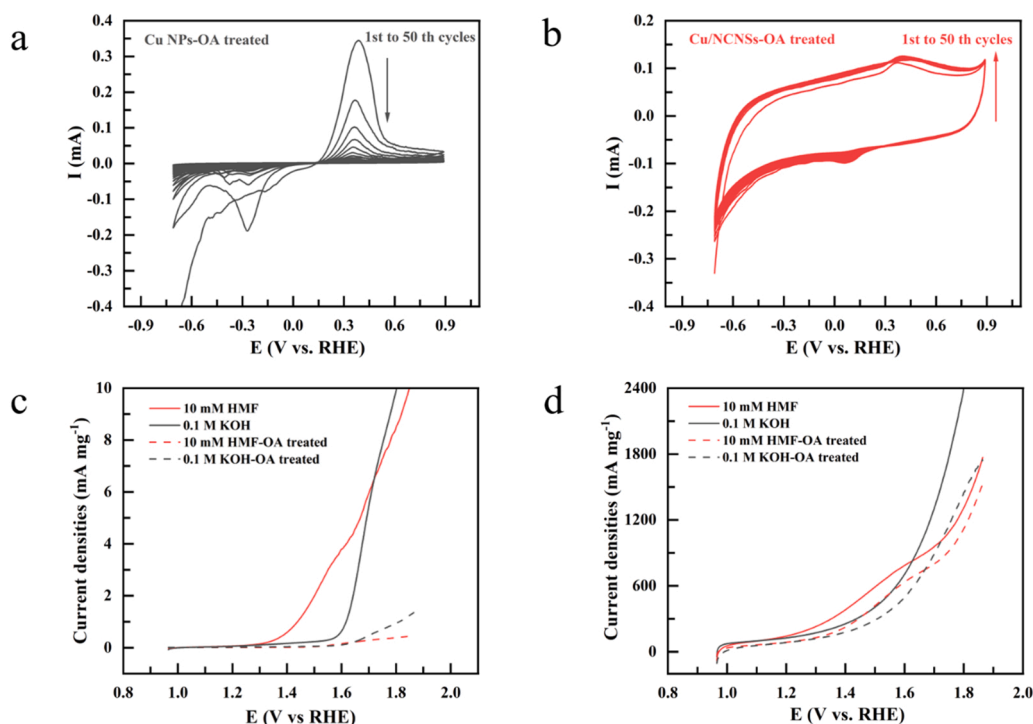


**Fig. 4.** 50-cycle CV measurements in 0.1 M KOH + 0.1 M OA solutions over (a) Cu NPs and (b) Cu/NCNs. LSV curves of HMFOR and OER on (c) Cu NPs and (d) Cu/NCNs before and after OA treatment.

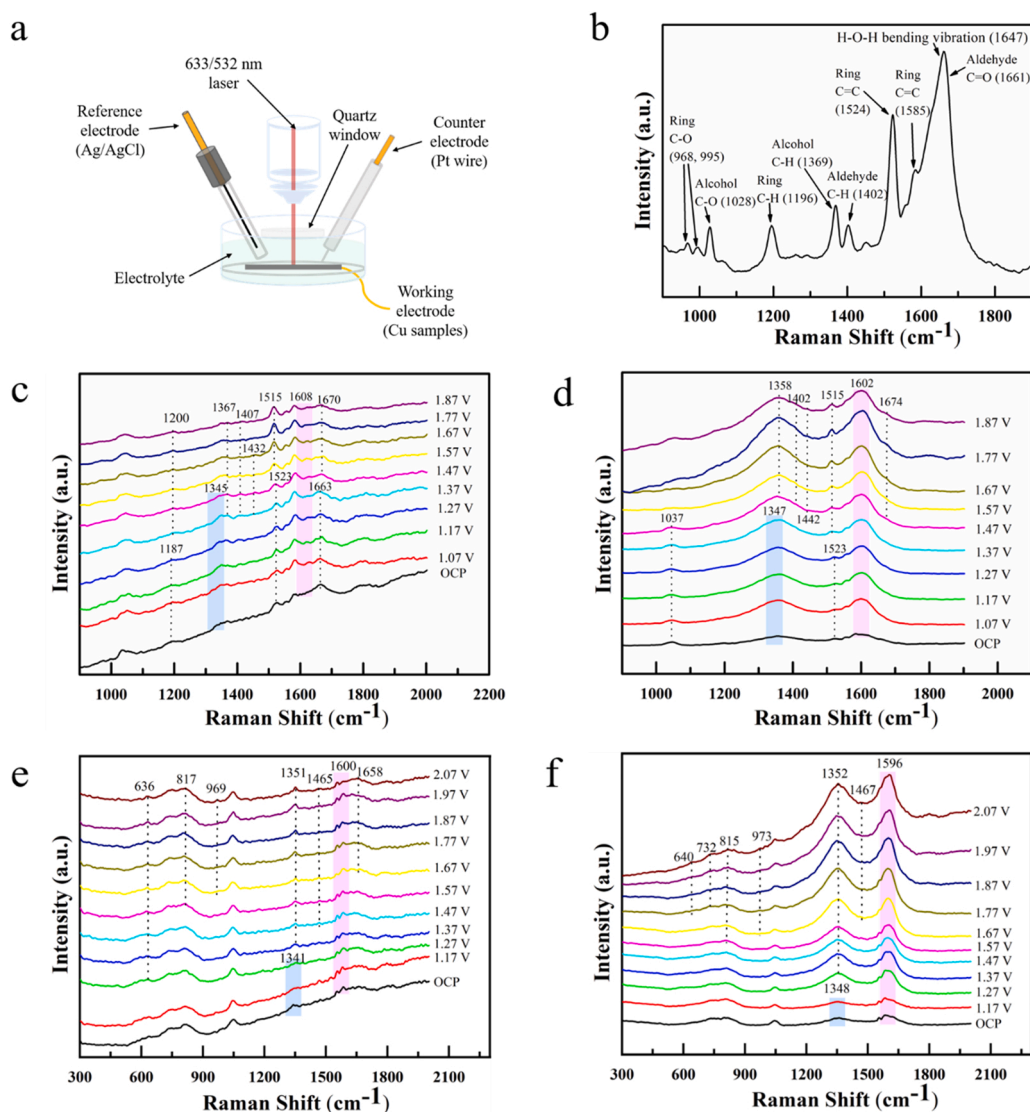
Cu/NCNs shown in Fig. 1d reveals the presence of mesopores in the sample. The Cu/NCNs has a Brunauer–Emmett–Teller (BET) surface area of 120.8 m<sup>2</sup> g<sup>-1</sup>. The Raman spectra shown in Fig. 1e show two characteristic peaks, which are associated with the D and G bands of the carbon materials. The intensity ratio ( $I_D/I_G$ ) of Cu/NCNs is 0.96, which is identical to that of NCNs.

Fig. 2a shows the normalized X-ray absorption near edge structure (XANES) spectra of the Cu K<sub>3</sub>-edge for the Cu/NCNs along with Cu foil, CuO and Cu<sub>2</sub>O references. The position of the absorption edge for the Cu/NCNs is close to those of CuO and Cu<sub>2</sub>O, suggesting that the oxidation state of Cu in the Cu/NCNs is between Cu<sup>1+</sup> and Cu<sup>2+</sup> [29, 30]. Fig. 2b shows the  $k^3$ -weighted Fourier transform spectra in R space of the Cu K-edge extended X-ray absorption fine structure (FT-EXAFS) of the sample. The Cu/NCNs display a main peak at  $\approx 1.5$  Å, corresponding to the Cu–N coordination [31]. No Cu–Cu peak (at 2.2 Å) was detected, suggesting that the Cu atoms are predominantly bonded with N atoms in the Cu/NCNs, which is consistent with the HAADF-STEM and XRD results. This result can be further confirmed by the wavelet transform (WT) results as shown in Fig. 2c. It can be seen that the WT contour plot of Cu/NCNs presents only one maximum intensity at 4.5 Å<sup>-1</sup>, which is assigned to the Cu–N/C coordination. An intensity maximum at 7.2 Å<sup>-1</sup> associated with Cu–Cu coordination is not detected, and the shape of the intensity maximum for Cu/NCNs is different from that of Cu–O coordination in CuO. These results suggest that no Cu or CuO nanoparticles is present in Cu/NCNs. EXAFS fitting results (see Fig. 2d and e) reveal that the average coordination number is 4.8 and that the average bond distance of Cu–N is 1.98 Å for the Cu–N<sub>x</sub> species. The voltammograms shown in Fig. S2 also indicate that Cu nanoparticles are not present in the samples because the CV curves of Cu/NCNs are very similar to those of NCNs, and no peaks related to Cu redox are observed.

### 3.2. Electrocatalytic performance of Cu/NCNs

To highlight the critical role of single copper atoms, LSV tests were first performed in 0.1 M KOH + 10 mM HMF solutions (see Fig. 3a). The

current density of NCNs for HMF oxidation reaction (HMFOR) is negligible. Cu NPs also have poor catalytic activity towards OER and HMFOR as the current densities are only 0.23 and 2.06 mA mg<sup>-1</sup>, respectively, at 1.50 V (see Fig. 3b). In contrast, by transitioning to atomic level, the Cu/NCNs exhibit current densities of 653.2 and 442.5 mA mg<sup>-1</sup> for HMFOR and OER, respectively (see Fig. 3c). To verify the universality of the single-copper-atom electrocatalyst, the electro-oxidation of aldehydes (Fur, GLU and FM), alcohols (MA, EtOH, IA, EG, GLY and BA), and acids (FA and OA) by Cu/NCNs were studied by LSV (see Fig. S3) measurements. A further inspection reveals that the current densities of electro-oxidation of Fur, MA, EtOH and IA are lower than the OER current density, indicating that the Cu/NCNs is not a promising electrocatalyst for transformation of these compounds. The current densities of FA and OA oxidation on the Cu/NCNs are slightly higher than that of OER, which is contrary to the result obtained from Cu NPs (see Fig. S4). For a better comparison, the onset potentials and current densities of the Cu/NCNs and Cu NPs at 1.6 V are depicted in Fig. 3d and e, respectively. Compared with Cu NPs, the Cu/NCNs have a lower onset potential and larger current density for both HMFOR and OER. The onset potentials of MA, EtOH, and IA oxidation on the Cu/NCNs are higher than that of OER, while the onset potentials of GLY, GLU, HMF, Fur, FM, BA, EG, FA, and OA oxidation are lower than that of OER. Especially, the electro-oxidation of GLU on Cu/NCNs shows the minimum onset potential of 1.13 V, which is much lower than that obtained from Cu NPs (1.32 V). The onset potentials for GLY, HMF, and BA oxidation on Cu/NCNs are 1.18, 1.23, and 1.20 V, respectively, corresponding to 1.20, 1.35, and 1.39 V obtained from Cu NPs. Besides, the Cu/NCNs possess a maximum current density of 2354.5 mA mg<sup>-1</sup> for GLU oxidation at 1.60 V, which is 643 times that of Cu NPs. The current densities of GLY, HMF and FM oxidation are 2234.7, 846.1, 1669.7 mA mg<sup>-1</sup>, respectively, which are 253, 222, and 448 times those of Cu NPs. The larger current densities resulted from Cu/NCNs suggest that the single copper atoms anchored on NCNs afforded abundant active sites for the substrate oxidation and significantly promoted the reactions. Fig. 3f shows current densities and TOF values of GOR on Cu/NCNs at three applied potentials. Increasing potential from 1.27 to



**Fig. 5.** In-situ electrochemical Raman spectra of HMF and GLY oxidation. (a) Schematic diagram for in-situ Raman measurements. (b) Raman spectrum of 10 mM HMF solutions. In-situ electrochemical Raman spectra on (c) Cu NPs and (d) Cu/NCNSs recorded in 0.1 M KOH + 10 mM HMF solutions. In-situ electrochemical Raman spectra on (e) Cu NPs and (f) Cu/NCNSs recorded in 0.1 M KOH + 100 mM GLY solutions.

1.67 V, GLY current density greatly increases from 282.3 to 2270.1 mA mg<sup>-1</sup>. The TOF values are 0.07, 0.45 and 0.56 s<sup>-1</sup> at the three potentials, which are 2.3, 7.5 and 2.8 times that of OER, respectively, manifesting an excellent GOR performance of the Cu/NCNSs.

The products of HMF, Fur, GLY, MA and OA oxidation over the Cu/NCNSs were analyzed by HPLC. The representative i-t curves of HMF (see Fig. S5a) and GLY (see Fig. S5b) oxidation on Cu/NCNSs and Cu NPs were recorded. The concentrations of the substrates and products were determined based on the calibrated curves as shown in Fig. S6–8. To exclude the catalytic effect of the NCNSs, the products of HMF oxidation on NCNSs were first detected. The amounts of products produced by NCNSs are negligible (see Table S1 and Fig. S9). Fig. S10–15 show the representative HPLC curves to illustrate the conversion of the substrates. The product selectivities of HMF (see Fig. 3 g and h) and GLY oxidation (see Fig. 3 i and j) were determined. Cu NPs produce plenty of FFCA and FDCA, and a few DFF and HFCA at the three potentials (see Fig. 3 g). Compared with the Cu NPs, the Cu/NCNSs yield more FFCA but less FDCA at lower potentials (see Fig. 3 h). Notably, a maximum FFCA selectivity of 67% is obtained as the reaction is carried out at 1.57 V for 1 h. When the reaction time is over 1 h, the selectivity of FFCA decreases while that of DFF increases with increasing potential. The conversion

rates of HMF oxidation on the Cu/NCNSs and Cu NPs are shown in Fig. S16. For GLY oxidation, Cu NPs generate more FA at lower potentials but the selectivity decreases with increasing potentials and reaction time (see Fig. 3i). GLOA selectivity increases with increasing reaction time, leading to a maximum value of 51.4% at 1.47 V for 4 h. The Cu/NCNSs also produce more FA, and FA selectivities at the three potentials are close to 100% for 1 h (see Fig. 3j). Increasing the reaction time, the selectivity of GLOA gradually increases under higher potentials, and a maximum value of 58.0% is obtained at 1.47 V for 4 h, indicating that higher potentials are favorable for the generation of GLOA. A maximum GLY conversion of 66.4% is obtained from the Cu/NCNSs at 1.47 V for 4 h (see Fig. S17), which is much higher than those reported in recent work [32–38]. When the Cu/NCNSs were used for Fur and MA oxidation, the concentrations of the corresponding products 2-FA and FA are much smaller than those obtained from Cu NPs (see Fig. S18 and 19), suggesting that the Cu/NCNSs have limited effects on Fur and MA oxidation. Since the product of OA oxidation (i.e., CO<sub>3</sub><sup>2-</sup>) is difficult to be detected by HPLC, OA concentration was monitored. OA concentrations remain almost unchanged throughout the reaction (see Fig. S20a and Fig. S20b), indicating that the activity of Cu/NCNSs and Cu NPs on OA oxidation is negligible.

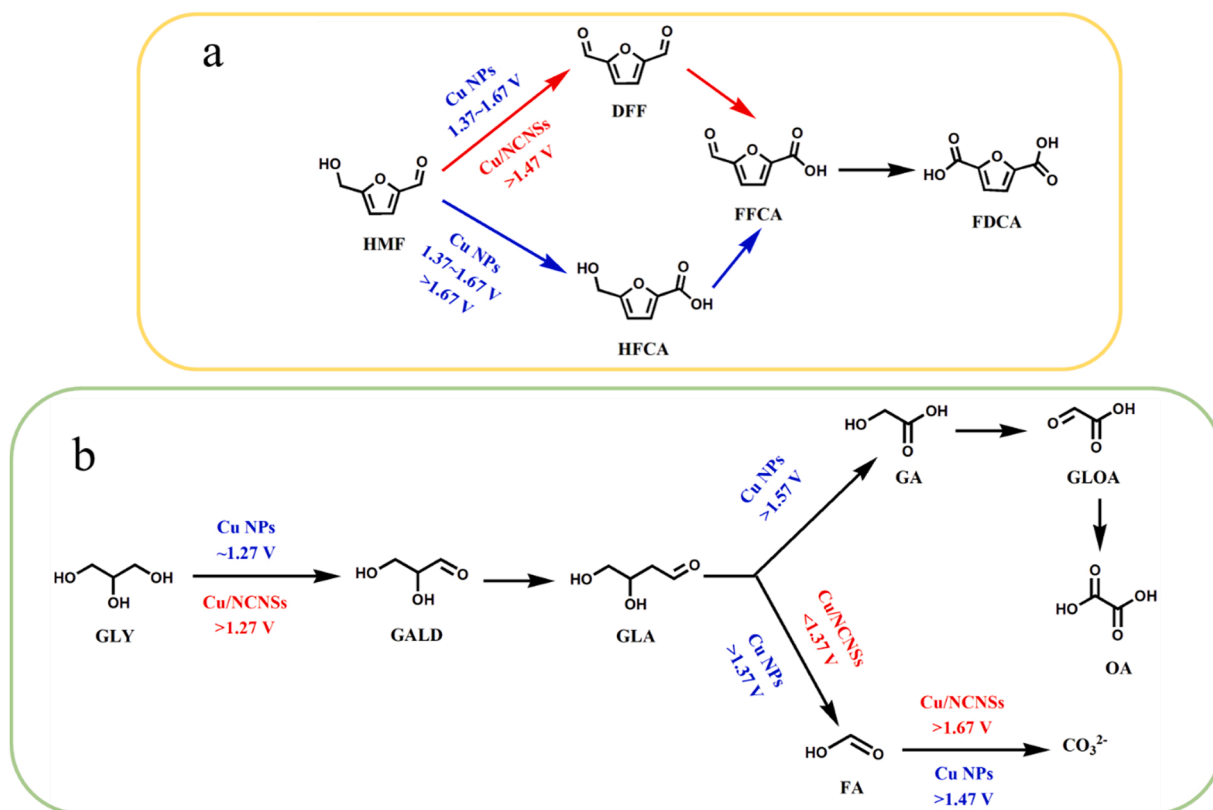


Fig. 6. Proposed reaction pathway of (a) HMF and (b) GLY electro-catalytic oxidation on Cu/NCNSs and Cu NPs in alkaline solutions. Blue and red colors are considered to be the dominant pathways for Cu NPs and Cu/NCNSs, respectively.

### 3.3. Effects of OA passivator on HMF oxidation

Since it was reported that OA is capable of inhibiting the oxidation of copper surfaces [39,40], in this work, it was employed as a probe to explore the active sites of Cu/NCNSs and Cu NPs for HMF oxidation. After cycling Cu NPs in 0.1 M KOH + 0.1 M OA solution, the intensity of the peaks related to copper redox decreases sharply, and the peak almost disappears after 50 cycles (see Fig. 4a). This indicates that a passivation layer is formed on the copper surface after OA treatment, which inhibits the oxidation of copper [40,41]. Unlike the Cu NPs, two peaks are noted from the CV curves of the Cu/NCNSs and NCNSs, and their intensities gradually increase with the number of cycles (see Fig. 4b and Fig. S21). These results further verify that the copper in the Cu/NCNSs is present as a form of single atoms rather than nanoparticles. The effects of OA passivator on HMF oxidation were subsequently studied by LSV measurements (see Fig. 4c and d). After OA treatment, the current density of HMFOR on the Cu NPs is significantly dropped, leading to negligible catalytic activity of OA-treated Cu NPs for HMFOR. Such a phenomenon can also be observed from the OER, implying that HMFOR and OER may share some common active sites. After OA treatment, the surface of Cu NPs was passivated, inhibiting the formation of high-valence states of copper which serves as active sites for HMFOR and OER. For the Cu/NCNSs, the activities of HMFOR and OER after OA treatment slightly decrease, indicating that OA possesses limited effects on the single copper atoms.

### 3.4. In-situ electrochemical Raman spectra

It is demonstrated that the Cu/NCNSs possess excellent catalytic activity for HMF and GLY oxidation, but is less active for Fur, MA and OA oxidation. To gain further insights on the adsorption and transformation processes of the five compounds on the SAEC, operando electrochemical Raman spectra were performed using a custom-built

spectro-electrochemical cell as shown in Fig. 5a. Fig. 5b and Fig. S22-24 show the ex-situ spectra of HMF, GLY, Fur, MA, OA and their possible oxidation products, and the bands in the spectra are assigned on the basis of established experimental and theoretical studies [42-51]. To exclude the Raman adsorption of water molecules, Raman spectroscopy was first performed on ultrapure water and 0.1 M KOH solutions. A peak at  $\sim 1640\text{ cm}^{-1}$  is clearly observed (see Fig. S25), which is associated with the bending vibration of H-O-H bonds in water molecules [52]. This implies that the C=O stretching vibration ( $\sim 1660\text{ cm}^{-1}$ ) of the substrate or oxidation product may be interfered by water. During the tests, the i-t curves (see Fig. S26) and electron micrographs (see Fig. S27 and 28) of the samples were also recorded. Fig. 5c shows the in-situ electrochemical Raman spectra of HMF oxidation on the Cu NPs. When the potential is over 1.27 V, a peak at  $1187\text{ cm}^{-1}$  associated with the C-H of furan rings is positively shifted to  $1200\text{ cm}^{-1}$ , suggesting the formation of the product HFCA [43]. Meanwhile, a peak at  $1432\text{ cm}^{-1}$  related to aldehyde C-H is noted, which is the characteristic peak of product DFF [53]. As the potential is over 1.67 V, the DFF-related peak disappears. Therefore, it can be inferred that when the potential is lower than 1.67 V, HMF oxidation on Cu NPs may follow two oxidation pathways, namely, the aldehyde oxidation pathway and hydroxyl oxidation pathway. In contrast, when the potential is higher than 1.67 V, the reaction proceeds along the path of HFCA generation (see Fig. 6a). Two peaks at  $1367$  and  $1407\text{ cm}^{-1}$  appearing from 1.37 V are related to the C-H adjacent to alcohol and aldehyde of the product FFCA [53,54], respectively. Notably, a peak at  $1663\text{ cm}^{-1}$  associated with the aldehyde groups of HMF molecules appears at open circuit potential (OCP) [5,43], but its intensity is weakened and positively shifted to  $1670\text{ cm}^{-1}$  when the potential is over 1.37 V. This may be due to the interaction of HMF molecules with the active sites [43]. As the potential increases, the C=C of the furan ring-related peak at  $1523\text{ cm}^{-1}$  negatively shifted to  $1515\text{ cm}^{-1}$ , which is attributed to the conversion of HMF to FFCA. The peaks at  $1345$  and  $1608\text{ cm}^{-1}$  are ascribed to the D and G bands of the

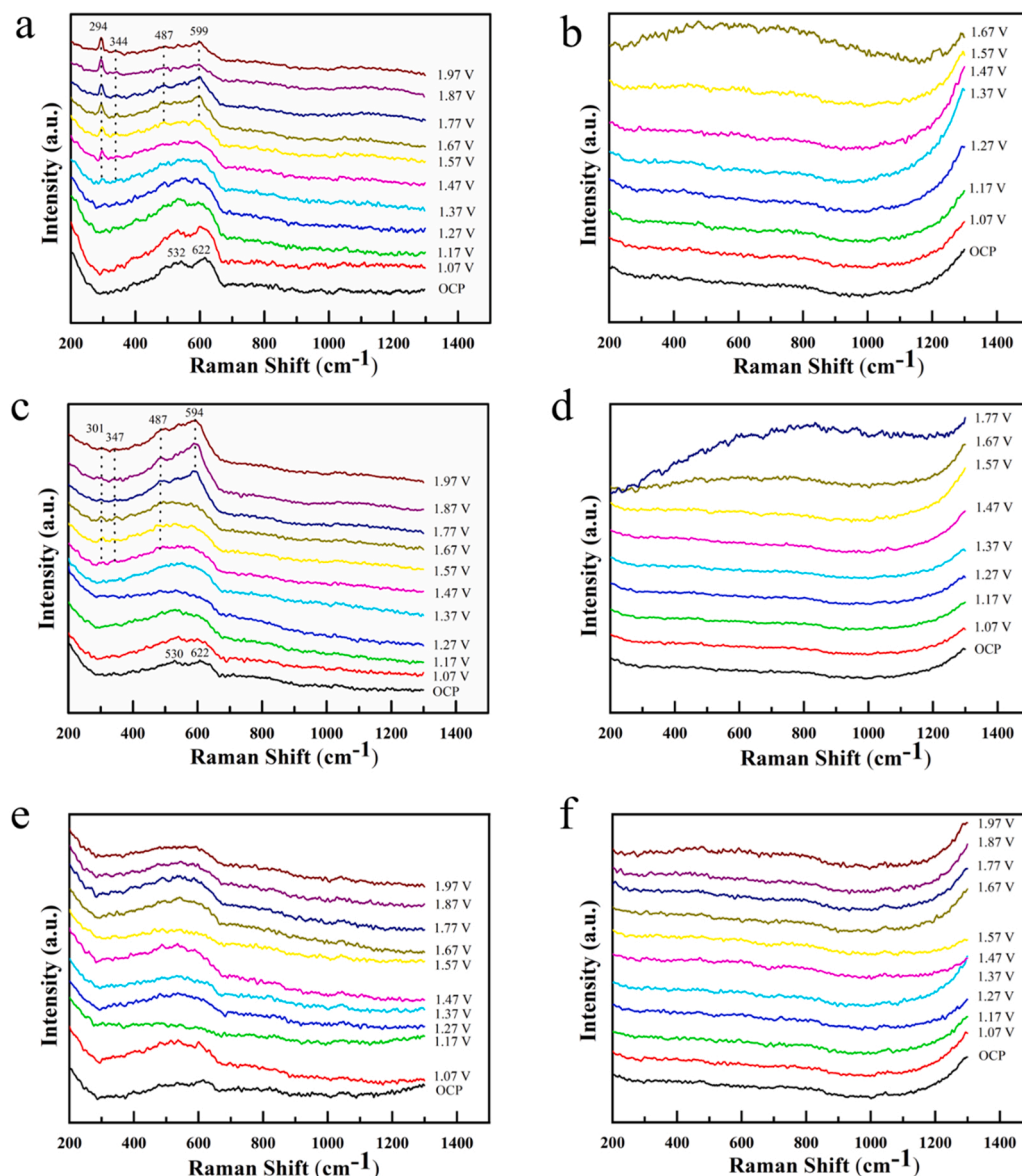


Fig. 7. In-situ electrochemical Raman spectra of water (a and b), HMF (c and d) and GLY (e and f) oxidation on Cu NPs and Cu/NCNSs, respectively.

carbon paper [43].

When the Cu/NCNSs were used, the position of C-O adjacent to the alcohol group is positively shifted to  $1037\text{ cm}^{-1}$  relative to the solution spectrum (see Figs. 5b and 5d), indicating the interaction of the alcohol groups with the single copper atoms. At potentials over  $1.47\text{ V}$ , the DFF related peak at  $1442\text{ cm}^{-1}$  is observed whilst the peak of alcohol at  $1037\text{ cm}^{-1}$  disappears, which can be interpreted as a signature of the intermediate en route to DFF, that is, the transformation of alcohol groups to aldehyde groups [43]. The peaks associated with FFCA are negatively shifted to  $1358/1402\text{ cm}^{-1}$  and their appearance is delayed at  $1.47\text{ V}$ , indicating different adsorption modes of HMF molecules or intermediates on the Cu/NCNSs. The peak at  $1515\text{ cm}^{-1}$  related to FFCA appears at  $1.37\text{ V}$ , a much lower potential compared to that noted from the Cu NPs, indicating fast reaction kinetics on the Cu/NCNSs. Notably, no HFCA-related peaks are detected throughout the reaction, implying that HMF oxidation on the Cu/NCNSs follows an alcohol oxidation pathway (see Fig. 6a).

Fig. 5e shows the in-situ electrochemical Raman spectra of GLY oxidation over the Cu NPs. A peak at  $636\text{ cm}^{-1}$  is observed at  $1.27\text{ V}$ , corresponding to the bending vibration of C-C-O from the product GALD [42]. Above  $1.37\text{ V}$ , a peak at  $1351\text{ cm}^{-1}$  associated with the bending

vibration of C-H from the product FA is detected [42]. Increasing potential to  $1.47\text{ V}$ , a  $\text{CO}_3^{2-}$  related peak appears at  $1465\text{ cm}^{-1}$  [51], indicating the conversion of FA to carbonate. Above  $1.57\text{ V}$ , the Raman characteristic peaks of GA (C-C stretching), GLOA (C-C stretching) and OA (C=O stretching) are detected at  $817$ ,  $969$  and  $1658\text{ cm}^{-1}$  [42], respectively. For the Cu/NCNSs, the FA-related peak at  $1352\text{ cm}^{-1}$  appears earlier to  $1.37\text{ V}$  as shown in Fig. 5f, which may be related to the fact that the resulting GALD intermediate can be rapidly oxidized to FA on the surface of single copper atoms. A new peak related to the bending vibration of C-O-O from OA appears at  $732\text{ cm}^{-1}$ . The peak related to  $\text{CO}_3^{2-}$  appears at a higher potential ( $>1.67\text{ V}$ ) relative to that using Cu NPs, manifesting that FA produced by Cu/NCNSs is difficult to be further oxidized at lower potentials. The proposed GLY oxidation pathway on the two catalysts is displayed in Fig. 6b. Given that neither HPLC nor Raman spectra detected the product of DHA, it can be inferred that GLY oxidation on the Cu NPs and Cu/NCNSs follows the terminal hydroxyl oxidation pathway.

In-situ electrochemical Raman spectra of Fur oxidation over the Cu NPs and Cu/NCNSs were recorded (see Fig. S29). As shown in Fig. S29a, a peak at  $1472\text{ cm}^{-1}$  related to C=C rings is positively shifted to  $1480\text{ cm}^{-1}$  at potentials over  $1.47\text{ V}$ . This could be attributed to the



formation of 2-FA. This peak is also detected using the Cu/NCNSs (see Fig. S29b), and it appears at a relatively lower potential of 1.37 V as compared to that of Cu NPs. Except 2-FA, no other products are detected from the Raman spectra for the two catalysts, which is consistent with the HPLC results. The operando Raman spectra of MA oxidation on Cu NPs are shown in Fig. S30a. Two peaks at 639 and 1348  $\text{cm}^{-1}$  associated with the bending vibrations of C-O-O and C-H from the product FA are observed at 1.37 V, respectively. Notably, these two FA-related peaks are shifted to 643 and 1345  $\text{cm}^{-1}$  using the Cu/NCNSs. There are no peaks associated with OA oxidation product ( $\text{CO}_3^{2-}$ ) on the Cu/NCNSs and Cu NPs as shown in Fig. S31, indicating that the two catalysts have limited catalytic activity on OA oxidation, which is consistent with the HPLC results shown in Fig. S20.

Operando electrochemical Raman spectra tests were also performed to monitor the variations of the catalytic active sites. A laser with a wavelength of 633 nm was used as the excitation source. For clarity, in situ Raman spectra of carbon paper, NCNSs, and commercial nitrogen-doped graphene were first recorded in 0.1 M KOH (see Fig. S32). It reveals that the carbon substrates have no variations during the Raman tests. In 0.1 M KOH solutions, two broad peaks at 532 and 622  $\text{cm}^{-1}$  related to  $\text{Cu}_2\text{O}$  are first observed at OCP (see Fig. 7a) [55]. Above 1.37 V, two additional peaks related to CuO are observed at 294 and 344  $\text{cm}^{-1}$  [56]. Increasing the potential to 1.57 V, two peaks at 487 and 599  $\text{cm}^{-1}$ , corresponding to  $\text{Cu}(\text{OH})_2$  and  $\text{Cu}(\text{III})$  [55] species, respectively, start to appear. CuO,  $\text{Cu}(\text{OH})_2$  and  $\text{Cu}(\text{III})$  species were reported to be catalytically active for evolving  $\text{O}_2$  [55]. In contrast, the Raman spectra of the Cu/NCNSs show no significant variations over the applied potential range (see Fig. 7b), manifesting that the active Cu-N<sub>x</sub> species in the Cu/NCNSs remain intact during the electrochemical process. This also confirms that there are no nanoparticles in the Cu/NCNSs sample. After adding 10 mM HMF into the electrolytes, the intensities of the peaks associated with CuO are weakened (see Fig. 7c), and their appearance is delayed at 1.47 V. The peak at 487  $\text{cm}^{-1}$  related to  $\text{Cu}(\text{OH})_2$  appears earlier at 1.47 V and its intensity is enhanced. The peak related to  $\text{Cu}(\text{III})$  does not appear until the potential reaches to 1.77 V. Thus, it can be concluded that the main active species for HMF oxidation is  $\text{Cu}(\text{OH})_2$  while CuO and  $\text{Cu}(\text{III})$  are active for  $\text{OH}^-$  oxidation at high potentials. Using Cu/NCNSs for HMF oxidation, no Raman peaks are observed (see Fig. 7d).

When 0.1 M GLY was added to the electrolyte, the formation of CuO,  $\text{Cu}(\text{OH})_2$  and  $\text{Cu}(\text{III})$  of Cu NPs is suppressed due to surface binding [12] (see Fig. 7e). Therefore, it is surmised that the three active species are all active for GLY oxidation. Similar to HMF oxidation, no peaks are detected from GLY oxidation by Cu/NCNSs (see Fig. 7f). When Cu NPs are used for Fur and MA oxidation, all the CuO,  $\text{Cu}(\text{OH})_2$  and  $\text{Cu}(\text{III})$  species are observed, but their appearance is delayed at higher potentials (see Fig. S33a and S34a). Additionally, no obvious Raman peaks are detected for Fur and MA oxidation on the Cu/NCNSs (see Fig. S33b and S34b).

#### 4. Conclusions

In summary, a single copper atom electrocatalyst supported by nitrogen-doped carbon nanosheets was evaluated for biomass conversion. Electrochemical measurements show that the Cu/NCNSs possess excellent catalytic performance for GLY, GLU, HMF, FM, EG and BA oxidation. A highest FFCA selectivity (67%) and a maximum FA selectivity (100%) were obtained from the Cu/NCNSs catalyst, but only a small amount of product was produced from MA and FA oxidation. The concentration of OA during HPLC measurements remained unchanged, and no Raman peaks related to its oxidation product were detected on both the Cu/NCNSs and Cu NPs catalysts. It reveals that the activity of OA oxidation on the two catalysts are both limited. On the basis of in-situ Raman spectra and HPLC results, it could be concluded that HMF oxidation on Cu NPs followed the path to DFF at lower potentials, while it turned to HFCA path when the applied potential was high than 1.67 V.

For the Cu/NCNSs, HMF oxidation followed the alcohol hydroxyl oxidation pathway, that is, the direction of generating DFF. The active sites on the Cu/NCNSs were significantly different from those on the Cu NPs. The findings reported in this work can broaden the application scope of SAECs in the field of biomass conversion, and afford new insights on the mechanisms of electro-oxidation of small molecules by SAECs.

#### CRedit authorship contribution statement

Y. Z. and Y. S. designed the experimental protocol. Y. Z. carried out the catalyst synthesis. Y. Z., Y. S., T. S., and X. L. carried out the physical characterization of the catalyst. Y. Z. carried out electrochemical and spectroscopic experiments. Y. Z. wrote the manuscript. Y. S. revised the manuscript.

#### Declaration of Competing Interest

The authors declare that they have no known competing financial interests or personal relationships that could have appeared to influence the work reported in this paper.

#### Data Availability

Data will be made available on request.

#### Acknowledgements

The project was financially supported by the National Natural Science Foundation of China (22279035), 111 Project (B17018) and a research grant (204-A021001) from the China-Singapore International Joint Research Institute.

#### Appendix A. Supporting information

Supplementary data associated with this article can be found in the online version at doi:10.1016/j.apcatb.2022.122218.

#### References

- [1] A.M. Bahmanpour, M. Signorile, O. Krocher, Recent progress in syngas production via catalytic  $\text{CO}_2$  hydrogenation reaction, *Appl. Catal. B* 295 (2021), 120319.
- [2] S.Q. Niu, X.P. Kong, S.W. Li, Y.Y. Zhang, J. Wu, W.W. Zhao, P. Xu, Low Ru loading  $\text{RuO}_2/(\text{Co,Mn})_3\text{O}_4$  nanocomposite with modulated electronic structure for efficient oxygen evolution reaction in acid, *Appl. Catal. B* 297 (2021), 120442.
- [3] W.L. Xu, C.J. Yu, J.Z. Chen, Z.Y. Liu, Electrochemical hydrogenation of biomass-based furfural in aqueous media by Cu catalyst supported on N-doped hierarchically porous carbon, *Appl. Catal. B* 305 (2022), 121062.
- [4] C.L. Chen, Z.Q. Zhou, J. Liu, B. Zhu, H.L. Hu, Y. Yang, G.X. Chen, M.R. Gao, J. Zhang, Sustainable biomass upgrading coupled with  $\text{H}_2$  generation over in-situ oxidized  $\text{Co}_3\text{O}_4$  electrocatalysts, *Appl. Catal. B* 307 (2022), 121209.
- [5] Y.F. Zhou, Y. Shen, H.Y. Li, Mechanistic study on electro-oxidation of 5-hydroxymethylfurfural and water molecules via operando surface-enhanced Raman spectroscopy coupled with an  $\text{Fe}^{3+}$  probe, *Appl. Catal. B* 317 (2022), 121776.
- [6] T.G. Vo, P.Y. Ho, C.Y. Chiang, Operando mechanistic studies of selective oxidation of glycerol to dihydroxyacetone over amorphous cobalt oxide, *Appl. Catal. B* 300 (2022), 120723.
- [7] Z.Y. Zhou, Y.N. Xie, L.Z. Sun, Z.M. Wang, W.K. Wang, L.Z. Jiang, X. Tao, L.N. Li, X. H. Li, G.H. Zhao, Strain-induced in situ formation of  $\text{NiOOH}$  species on Co-Co bond for selective electrooxidation of 5-hydroxymethylfurfural and efficient hydrogen production, *Appl. Catal. B* 305 (2022), 121072.
- [8] D. Li, Z.Y. Li, R. Zou, G. Shi, Y.M. Huang, W. Yang, W. Yang, C.F. Liu, X.W. Peng, Coupling overall water splitting and biomass oxidation via Fe-doped  $\text{Ni}_2\text{P}@C$  nanosheets at large current density, *Appl. Catal. B* 307 (2022), 121170.
- [9] Y.K. Song, W.F. Xie, Y.J. Song, H. Li, S.J. Li, S. Jiang, J.Y. Lee, M.F. Shao, Bifunctional integrated electrode for high-efficient hydrogen production coupled with 5-hydroxymethylfurfural oxidation, *Appl. Catal. B* 312 (2022), 121400.
- [10] R.P. Luo, Y.Y. Li, L.X. Xing, R.Y. Zhong, Z.Y. Qian, G.P. Yin, Y.C. Wang, L. Du, A dynamic  $\text{Ni}(\text{OH})(2)-\text{NiOOH}/\text{NiFeP}$  heterojunction enabling high-performance E-upgrading of hydroxymethylfurfural, *Appl. Catal. B* 311 (2022), 121357.
- [11] N. Zhang, Y. Zou, L. Tao, W. Chen, L. Zhou, Z. Liu, B. Zhou, G. Huang, H. Lin, S. Wang, Electrochemical oxidation of 5-hydroxymethylfurfural on nickel nitride/carbon nanosheets: reaction pathway determined by In situ sum frequency

- generation vibrational spectroscopy, *Angew. Chem. Int. Ed.* 58 (2019) 15895–15903.
- [12] B. Zhou, Y. Li, Y. Zou, W. Chen, W. Zhou, M. Song, Y. Wu, Y. Lu, J. Liu, Y. Wang, S. Wang, Platinum modulates redox properties and 5-hydroxymethylfurfural adsorption kinetics of Ni(OH)<sub>2</sub> for biomass upgrading, *Angew. Chem. Int. Ed.* 60 (2021) 22908–22914.
- [13] Y. Zhou, Y. Shen, J. Xi, Seed-mediated synthesis of Pt<sub>3</sub>Au<sub>5</sub>@Ag electrocatalysts for the selective oxidation of glycerol, *Appl. Catal. B* 245 (2019) 604–612.
- [14] B. Zhu, C.L. Chen, L.Y. Huai, Z.Q. Zhou, L. Wang, J. Zhang, 2,5-Bis(hydroxymethyl) furan: a new alternative to HMF for simultaneously electrocatalytic production of FDCA and H<sub>2</sub> over CoOOH/Ni electrodes, *Appl. Catal. B* 297 (2021), 120396.
- [15] X.H. Deng, M. Li, Y. Fan, L. Wang, X.Z. Fu, J.L. Luo, Constructing multifunctional 'Nanoplatelet-on-Nanoarray' electrocatalyst with unprecedented activity towards novel selective organic oxidation reactions to boost hydrogen production, *Appl. Catal. B* 278 (2020), 119339.
- [16] Y. Lu, T. Liu, C.L. Dong, Y.C. Huang, Y. Li, J. Chen, Y. Zou, S. Wang, Tuning the selective adsorption site of biomass on Co<sub>3</sub>O<sub>4</sub> by Ir single atoms for electrosynthesis, *Adv. Mater.* 33 (2021), e2007056.
- [17] D.-H. Nam, B.J. Taitt, K.-S. Choi, Copper-based catalytic anodes to produce 2,5-furandicarboxylic acid, a biomass-derived alternative to terephthalic acid, *ACS Catal.* 8 (2018) 1197–1206.
- [18] J. Zhang, Y. Shen, Electro-oxidation of glycerol into formic acid by nickel-copper electrocatalysts, *J. Electrochem. Soc.* 168 (2021), 084510.
- [19] Y. Wang, H. Su, Y. He, L. Li, S. Zhu, H. Shen, P. Xie, X. Fu, G. Zhou, C. Feng, D. Zhao, F. Xiao, X. Zhu, Y. Zeng, M. Shao, S. Chen, G. Wu, J. Zeng, C. Wang, Advanced electrocatalysts with single-metal-atom active sites, *Chem. Rev.* 120 (2020) 12217–12314.
- [20] B. Pattengale, Y. Huang, X. Yan, S. Yang, S. Younan, W. Hu, Z. Li, S. Lee, X. Pan, J. Gu, J. Huang, Dynamic evolution and reversibility of single-atom Ni(II) active site in 1T-MoS<sub>2</sub> electrocatalysts for hydrogen evolution, *Nat. Commun.* 11 (2020) 4114.
- [21] K. Shah, R. Dai, M. Mateen, Z. Hassan, Z. Zhuang, C. Liu, M. Israr, W.-C. Cheong, B. Hu, R. Tu, C. Zhang, X. Chen, Q. Peng, C. Chen, Y. Li, Cobalt single atom incorporated in ruthenium oxide sphere: a robust bifunctional electrocatalyst for HER and OER, *Angew. Chem. Int. Ed.* 61 (2022), e202114951.
- [22] Y. Chen, R. Gao, S. Ji, H. Li, K. Tang, P. Jiang, H. Hu, Z. Zhang, H. Hao, Q. Qu, X. Liang, W. Chen, J. Dong, D. Wang, Y. Li, Atomic-level modulation of electronic density at cobalt single-atom sites derived from metal-organic frameworks: enhanced oxygen reduction performance, *Angew. Chem. Int. Ed.* 60 (2021) 3212–3221.
- [23] Y. Kong, Y. Li, X. Sang, B. Yang, Z. Li, S. Zheng, Q. Zhang, S. Yao, X. Yang, L. Lei, S. Zhou, G. Wu, Y. Hou, Atomically dispersed Zinc(I) active sites to accelerate nitrogen reduction kinetics for ammonia electrosynthesis, *Adv. Mater.* 34 (2022) 2103548.
- [24] Y. Cai, J. Fu, Y. Zhou, Y.-C. Chang, Q. Min, J.-J. Zhu, Y. Lin, W. Zhu, Insights on forming N<sub>2</sub>O-coordinated Cu single-atom catalysts for electrochemical reduction CO<sub>2</sub> to methane, *Nat. Commun.* 12 (2021) 586.
- [25] W. Chen, X. Luo, T.J.A. Slater, Y. Zhou, S. Ling, R. Bao, J. Alves Fernandes, J. Wang, Y. Shen, General synthesis of single atom electrocatalysts via a facile condensation-carbonization process, *J. Mater. Chem. A* 8 (2020) 25959–25969.
- [26] Y. Zhou, Y. Shen, J. Piao, Sustainable conversion of glycerol into value-added chemicals by selective electro-oxidation on Pt-based catalysts, *ChemElectroChem* 5 (2018) 1636–1643.
- [27] Y. Zhou, Y. Shen, X. Luo, Critical practices in conducting electrochemical conversion of 5-hydroxymethylfurfural, *Catal. Sci. Technol.* 11 (2021) 4882–4888.
- [28] Y. Zhou, Y. Shen, X. Luo, Optimizing the activity and selectivity of glycerol oxidation over core-shell electrocatalysts, *J. Catal.* 381 (2020) 130–138.
- [29] Y. Li, B. Li, D. Zhang, L. Cheng, Q. Xiang, Crystalline carbon nitride supported copper single atoms for photocatalytic CO<sub>2</sub> reduction with nearly 100% CO selectivity, *ACS Nano* 14 (2020) 10552–10561.
- [30] S. Ma, Z. Han, K. Leng, X. Liu, Y. Wang, Y. Qu, J. Bai, Ionic exchange of metal-organic frameworks for constructing unsaturated copper single-atom catalysts for boosting oxygen reduction reaction, *Small* 16 (2020), e2001384.
- [31] T. Zhu, Q. Chen, P. Liao, W. Duan, S. Liang, Z. Yan, C. Feng, Single-atom Cu catalysts for enhanced electrocatalytic nitrate reduction with significant alleviation of nitrite production, *Small* 16 (2020), e2004526.
- [32] Y. Holade, C. Morais, K. Servat, T.W. Napporn, K.B. Kokoh, Toward the electrochemical valorization of glycerol: fourier transform infrared spectroscopic and chromatographic studies, *ACS Catal.* 3 (2013) 2403–2411.
- [33] M.S.E. Houache, A. Shubair, M.G. Sandoval, R. Safari, G.A. Botton, P.V. Jasen, E. A. González, E.A. Baranova, Influence of Pd and Au on electrochemical valorization of glycerol over Ni-rich surfaces, *J. Catal.* 396 (2021) 1–13.
- [34] S. Feng, J. Yi, H. Miura, N. Nakatani, M. Hada, T. Shishido, Experimental and theoretical investigation of the role of bismuth in promoting the selective oxidation of glycerol over supported Pt–Bi catalyst under mild conditions, *ACS Catal.* 10 (2020) 6071–6083.
- [35] J. Han, Y. Kim, D.H.K. Jackson, H. Chang, H.W. Kim, J. Lee, J.-R. Kim, Y. Noh, W. B. Kim, K.-Y. Lee, H.J. Kim, Enhanced catalytic performance and changed reaction chemistry for electrochemical glycerol oxidation by atomic-layer-deposited Pt-nanoparticle catalysts, *Appl. Catal. B* 273 (2020), 119037.
- [36] D. Lee, Y. Kim, H. Han, W.B. Kim, H. Chang, T.-M. Chung, J.H. Han, H.W. Kim, H. J. Kim, Atomic-layer-deposited SnO<sub>2</sub> on Pt/C prevents sintering of Pt nanoparticles and affects the reaction chemistry for the electrocatalytic glycerol oxidation reaction, *J. Mater. Chem. A* 8 (2020) 15992–16005.
- [37] Y. Kim, H.W. Kim, S. Lee, J. Han, D. Lee, J.-R. Kim, T.-W. Kim, C.-U. Kim, S.-Y. Jeong, H.-J. Chae, B.-S. Kim, H. Chang, W.B. Kim, S.M. Choi, H.J. Kim, The role of ruthenium on carbon-supported PtRu catalysts for electrocatalytic glycerol oxidation under acidic conditions, *ChemCatChem* 9 (2017) 1683–1690.
- [38] N. Benipal, J. Qi, Q. Liu, W. Li, Carbon nanotube supported PdAg nanoparticles for electrocatalytic oxidation of glycerol in anion exchange membrane fuel cells, *Appl. Catal. B* 210 (2017) 121–130.
- [39] J. Peng, B.L. Chen, Z.C. Wang, J. Guo, B.H. Wu, S.Q. Hao, Q.H. Zhang, L. Gu, Q. Zhou, Z. Liu, S.Q. Hong, S.F. You, A. Fu, Z.F. Shi, H. Xie, D.Y. Cao, C.J. Lin, G. Fu, L.S. Zheng, Y. Jiang, N.F. Zheng, Surface coordination layer passivates oxidation of copper, *Nature* 586 (2020) 390.
- [40] Y.C. Ma, B.M. Fan, H. Liu, G.F. Fan, H. Hao, B. Yang, Enhanced corrosion inhibition of aniline derivatives electropolymerized coatings on copper: preparation, characterization and mechanism modeling, *Appl. Surf. Sci.* 514 (2020), 146086.
- [41] L.M.M. dos Santos, J.C. Lacroix, K.I. Chane-Ching, A. Adenier, L.M. Abrantes, P. C. Lacaze, Electrochemical synthesis of polypyrrole films on copper electrodes in acidic and neutral aqueous media, *J. Electroanal. Chem.* 587 (2006) 67–78.
- [42] C. Liu, M. Hirohara, T. Maekawa, R. Chang, T. Hayashi, C.-Y. Chiang, Selective electro-oxidation of glycerol to dihydroxyacetone by a non-precious electrocatalyst-CuO, *Appl. Catal. B* 265 (2020), 118543.
- [43] N. Heidary, N. Kornienko, Electrochemical biomass valorization on gold-metal oxide nanoscale heterojunctions enables investigation of both catalyst and reaction dynamics with operando surface-enhanced Raman spectroscopy, *Chem. Sci.* 11 (2020) 1798–1806.
- [44] H. Ghalla, N. Issaoui, M.V. Castillo, S.A. Brandán, H.T. Flakus, A complete assignment of the vibrational spectra of 2-furoic acid based on the structures of the more stable monomer and dimer, *Spectrochim. Acta A Mol. Biomol. Spectrosc.* 121 (2014) 623–631.
- [45] K.Z. Gaca-Zajac, B.R. Smith, A. Nordon, A.J. Fletcher, K. Johnston, J. Sefcik, Investigation of IR and Raman spectra of species present in formaldehyde-water-methanol systems, *Vib. Spectrosc.* 97 (2018) 44–54.
- [46] T. Jia, P. Li, Z. Shang, L. Zhang, T. He, Y. Mo, A study of surface enhanced Raman scattering for furfural adsorbed on silver surface, *J. Mol. Struct.* 873 (2008) 1–4.
- [47] E. Mendelovici, R.L. Frost, T. Klopogge, Cryogenic Raman spectroscopy of glycerol, *J. Raman Spectrosc.* 31 (2000) 1121–1126.
- [48] B. Hanoune, L. Paccou, P. Delcroix, Y. Guinet, Raman identification of H<sub>2</sub>CO in aqueous solutions, *J. Raman Spectrosc.* 42 (2011) 1202–1204.
- [49] A. Emin, A. Hushur, T. Mamtimin, Raman study of mixed solutions of methanol and ethanol, *AIP Adv.* 10 (2020), 065330.
- [50] B. Yang, X. Cao, H. Lang, S. Wang, C. Sun, Study on hydrogen bonding network in aqueous methanol solution by Raman spectroscopy, *Spectrochim. Acta A Mol. Biomol. Spectrosc.* 225 (2020), 117488.
- [51] W.R. Carper, P.G. Wahlbeck, T.R. Griffiths, DFT models of molecular species in carbonate molten salts, *J. Phys. Chem. B* 116 (2012) 5559–5567.
- [52] T.A. Dolenko, I.V. Churina, V.V. Fadeev, S.M. Glushkov, Valence band of liquid water Raman scattering: some peculiarities and applications in the diagnostics of water media, *J. Raman Spectrosc.* 31 (2000) 863–870.
- [53] N. Heidary, N. Kornienko, Operando vibrational spectroscopy for electrochemical biomass valorization, *Chem. Commun.* 56 (2020) 8726–8734.
- [54] N. Heidary, D. Chartrand, A. Guet, N. Kornienko, Rational incorporation of defects within metal-organic frameworks generates highly active electrocatalytic sites, *Chem. Sci.* 12 (2021) 7324–7333.
- [55] Y. Deng, A.D. Handoko, Y. Du, S. Xi, B.S. Yeo, In situ Raman spectroscopy of copper and copper oxide surfaces during electrochemical oxygen evolution reaction: identification of Cu-III oxides as catalytically active species, *ACS Catal.* 6 (2016) 2473–2481.
- [56] X. Pang, H. Bai, H. Zhao, W. Fan, W. Shi, Efficient electrocatalytic oxidation of 5-hydroxymethylfurfural coupled with 4-nitrophenol hydrogenation in a water system, *ACS Catal.* 12 (2022) 1545–1557.